INSTITUTE OF PHYSICS PUBLISHING PHYSICS IN MEDICINE AND BIOLOGY

Phys. Med. Biol. **50** (2005) 4863–4885 doi:10.1088/0031-9155/50/20/009

Development and validation of MCNP4C-based Monte Carlo simulator for fan- and cone-beam x-ray CT

Mohammad Reza Ay and Habib Zaidi

Division of Nuclear Medicine, Geneva University Hospital, CH-1211 Geneva 4, Switzerland

E-mail: habib.zaidi@hcuge.ch

Received 29 April 2005, in final form 1 July 2005
Published 5 October 2005
Online at stacks.iop.org/PMB/50/4863

Abstract

An x-ray computed tomography (CT) simulator based on the Monte Carlo N-particle radiation transport computer code (MCNP4C) was developed for simulation of both fan- and cone-beam CT scanners. A user-friendly interface running under Matlab 6.5.1 creates the scanner geometry at different views as MCNP4C's input file. The full simulation of x-ray tube, phantom and detectors with single-slice, multi-slice and flat detector configurations was considered. The simulator was validated through comparison with experimental measurements of different nonuniform phantoms with varying sizes on both a clinical and a small-animal CT scanner. There is good agreement between the simulated and measured projections and reconstructed images. Thereafter, the effects of bow-tie filter, phantom size and septa length on scatter distribution in fan-beam CT were studied in detail. The relative difference between detected total, primary and scatter photons for septa length varying between 0 and 95 mm is 11.2%, 1.9% and 84.1%, respectively, whereas the scatter-to-primary ratio decreases by 83.8%. The developed simulator is a powerful tool for evaluating the effect of physical, geometrical and other design parameters on scanner performance and image quality in addition to offering a versatile tool for investigating potential artefacts and correction schemes when using CT-based attenuation correction on dual-modality PET/CT units.

(Some figures in this article are in colour only in the electronic version)

1. Introduction

X-ray computed tomography (CT) images inherently have the tendency to produce physics-related artefacts compared to conventional planar radiography owing to the fact that the images are reconstructed from a large number of independent detector elements. The reconstruction algorithm often assumes that all these measurements are consistent; consequently any error of

measurement will usually be reflected as an error in the reconstructed images. There are several sources of error and artefact that affect clinical image quality in x-ray CT (Tofts and Gore 1980). It is therefore necessary to assess their significance and effect on the resulting images to reduce their impact either by optimizing the scanner design or by devising appropriate image correction and reconstruction algorithms. Recent advances in the design of fan- and cone-beam CT scanners rely on a detailed analysis of the influence of different physical and geometrical parameters on overall scanner performance, clinical image quality and patient absorbed dose. This could be achieved through costly physical experiments and development of test prototypes (Drangova and Fenster 1994, Lee *et al* 2003, Meinel *et al* 2003), analytical mathematical modelling (Siewerdsen and Jaffray 2000, De Man 2001, Chen and Ning 2002, De Francesco and Da Silva 2002, Hsieh 2003) or sophisticated Monte Carlo simulations (Colijn and Beekman 2004, Colijn *et al* 2004, Khodaverdi *et al* 2005). Although the investigation of imaging design parameters using the Monte Carlo method is time consuming compared to relatively simple mathematical modelling, the widespread availability of high performance parallel computing and more recently Grid technology in addition to the popularity of variance reduction techniques spurred the use of Monte Carlo calculations especially when modelling complex geometries. It should be noted that the accuracy of Monte Carlo simulations is well established in the area of CT dosimetry (Atherton and Huda 1995, Caon *et al* 1997, 1998, Wang *et al* 1999, Boone *et al* 2000, Jarry *et al* 2003, Lucas *et al* 2004).

One of the most important parameters in x-ray CT imaging is the bias induced by scattered radiation, which depends on the geometry of the CT scanner and the object under study. The amount and spatial distribution of the scatter component should be corrected for before or during the reconstruction process. Since the corruption of collected data with scattered photons decreases low contrast detectability, reduces CT number (Kanamori *et al* 1985) and introduces cupping and streak artefacts in the reconstructed images (Colijn and Beekman 2004), thorough knowledge of scatter distribution is essential for optimization of scanner design geometry (Siewerdsen and Jaffray 2000) and development of scatter correction techniques (Ohnesorge *et al* 1999).

The general practice of developing theoretical scatter models involves experimental physical measurements and mathematical modelling (Tofts and Gore 1980, Glover 1982, Johns and Yaffe 1982, Joseph and Spital 1982, Merritt and Chenery 1986, Siewerdsen and Jaffray 2001) whereas most recent publications focus on the use of Monte Carlo simulations (Kanamori *et al* 1985, Endo *et al* 2001, Malusek *et al* 2003, Colijn and Beekman 2004, Colijn *et al* 2004). It has long been recognized that the ideal research tool (gold standard) for scatter modelling and evaluation of scatter correction techniques is the Monte Carlo method. However, it should be emphasized that most studies were carried out using in-house developed dedicated Monte Carlo programs. The advantages offered by widely used and extensively tested state-of-the-art general-purpose Monte Carlo codes such as MCNP in terms of versatility, published reports and long-term technical support and maintenance are well established.

In this work, we have developed a Monte Carlo x-ray CT simulator for fan- and cone-beam geometries with single-slice, multi-slice and flat detector configurations based on the Monte Carlo N-particle (MCNP4C) radiation transport computer code. A user-friendly interface running under Matlab 6.5.1 (The MathWorks Inc., Natick, MA, USA) creates the geometry of the scanner in different views as MCNP4C input file. Detailed simulation of x-ray tube, collimator, bow-tie filter, phantom, detector geometry and material were considered. The simulator was validated through comparison with experimental measurements of different nonuniform phantoms with various sizes on both a clinical GE HiSpeed X/iF (General Electric Healthcare Technologies, Waukesha, WI, USA) fan-beam CT scanner and a small-animal SkyScan 1076 (SkyScan, Aartselaar, Belgium) cone-beam CT scanner. The accelerated

Monte Carlo simulator (AMCS) developed by Colijn *et al* (2004) was also used as a benchmark for validation of parameters difficult or impossible to measure experimentally. This paper addresses particularly some aspects not sufficiently covered in the literature, namely the assessment of scatter distribution in fan-beam scanners and the effect of scatter media (phantom size) and septa length up to 95 mm on the spatial distribution of scattered radiation. The aim is to exploit this tool for development and evaluation of scatter modelling and correction techniques in CT and assessment of potential sources of artefacts and their compensation when using CT-based attenuation correction in dual-modality PET/CT imaging (Hasegawa and Zaidi 2005).

2. Materials and methods

2.1. Description of the MCNP4C-based Monte Carlo CT simulator

2.1.1. The MCNP4C code. The x-ray CT simulator was built on top of the MCNP4C general-purpose Monte Carlo code, which serves as a core layer giving the opportunity to the developer to construct application-specific modules in a hierarchical layer architecture. MCNP is a general-purpose, continuous-energy, generalized-geometry, time-dependent, coupled neutron/photon/electron Monte Carlo transport code. For photon transport, the code takes into account photoelectric absorption, with the possibility of K- and L-shell fluorescent emission or Auger electron, coherent and incoherent scattering and pair production. The photoelectric cross sections are based on Storm and Israel (1967) whereas the scattering cross sections are taken from ENDF tabulations (Hubbell *et al* 1975). The continuous slowing down approximation energy loss model is used for electron transport. To improve the efficiency of electron and photon transport, two cards (PHYS:P and PHYS:E) are implemented in MCNP for biasing some physical parameters such as upper energy limit for electrons and photons (EMAX and EMCPF), production of secondary electrons by photons (IDES), coherent scattering (NOCOH), production of photons by electrons (IPHOT) and production of characteristic x-rays (XNUM).

In the first step, the user should create an input file which contains information about the problem such as geometry specification, description of materials, type of answer or tally and variance reduction techniques to be used. The geometry of MCNP treats an arbitrary three-dimensional configuration in Cartesian coordinate system. The number of cells in this code should be less than 10^5. If this limit is exceeded when using cell geometry, the lattice geometry should be used. The lattice uses a smaller number of cells but adds somewhat to the MCNP execution time. Important standard features that make MCNP very versatile and easy to use include a powerful general source and surface source, both geometry and output tally plotters, a rich collection of variance reduction techniques, a flexible tally structure and an extensive collection of cross-section data. For the purpose of decreasing computation time, MCNP takes advantage of parallel computer architectures. It is supported in multitasking mode on some mainframes and in multiprocessing mode on a cluster of workstations where the distributed processing uses the Parallel Virtual Machine (PVM) software (Briesmeister 2000).

2.1.2. User interface. The creation of input file in the MCNP4C code using first and second degree surfaces is not an easy task, especially when dealing with the complex geometries typical of an x-ray CT scanner requiring an extremely large number of plans to create detector cells and septa. The user interface running under Matlab 6.5.1 is realized by an easy to use concept. Basically, the user is asked to choose the x-ray CT scanner design parameters.

According to the information provided and options selected by user, the interface program creates the scanner geometry as input file for MCNP4C. Since MCNP is not able to simulate gantry rotation, the geometry of each view is created in separate files. To increase the performance of the simulator for investigation of different design parameters, the input file is created according to the parameters selected by the user, some of which are summarized in table 1. It should be emphasized that the number of detector rows were chosen to mimic typical geometry of prototype and commercially available CT scanners. There are two reasons for setting the number of detector elements in each row less than 1000 in the simulator. Firstly, the number of detector elements in all commercial single- and multi-slice fan-beam x-ray CT scanners is less then this value (between 800 and 900 elements) and secondly, as we aim at simulating the geometry of multi-slice scanners up to 64 slices and considering the limitation of MCNP4C in terms of number of cells (99'999), we made every effort to save the maximum number of cells for septa plates, voxel-based phantoms and other elements such as collimators and filters. It is, however, also possible to use more than 1000 elements per row in some cases if needed.

After simulation of all views, the sinogram is created from detector outputs after blank scan correction in all views by the user interface program. The filtered back-projection reconstruction algorithm was used for image reconstruction of the simulated data sets (Kak and Slaney 1999). Beam hardening effect, usually integrated in commercial software supplied by scanner manufacturers, was removed from the projections according to the method described by Kanamori *et al* (1985).

2.1.3. CT simulator features. The simulation process starts from the x-ray tube where the user interface offers two options for simulation of x-ray spectra. In the full simulation case, all electrons emitted from the filament are fully tracked into the target for the calculation of bremsstrahlung and produced characteristic photons (Ay *et al* 2004). Since tracking a large number of electrons into the target is time consuming, a pre-calculated spectra option offering the possibility of using spectra generated by different computational methods (Ay *et al* 2005) with varying focal spot size was implemented in the user interface program. In addition, the creation of simple shape-based and more complicated adult ORNL hermaphroditic mathematical phantoms (Cristy and Eckerman 1987) was also considered. The use of voxel-based phantoms as input to the simulator is still under development. One of the possibilities would be to use Scan2MCNP commercial program (White Rock Science, Los Alamos, NM, USA) to convert anatomical patient-specific CT or MRI data and other software phantoms (e.g. VIP-Man (Xu *et al* 2000)) to an input file for MCNP/MCNPX by paying special attention to the number of cells. For dosimetry purposes, the default value of PHYS:P and PHYS:E cards should be used to enable full electron and photon transport, while these parameters could be modified for imaging systems modelling purposes to speed-up the simulation process. The user interface program can create the input file as individual cells or as a lattice. This capability solves the limitation of MCNP in terms of number of cells especially for the cone-beam geometry with an extremely large number of detector elements. Different types of detector elements' output such as energy distribution of pulses created in each element (*F8 in MeV), photon fluence (F4 in cm^{-2}) and energy fluence (*F4 in MeV cm^{-2}) which pass through each element with various energy bins were considered in the simulator. The energy deposit per unit mass in each phantom's cell could be calculated using cell energy deposit tally (F6 in MeV g^{-1}) for dosimetry purposes. The four classes of variance reduction techniques (truncation, population control, modified sampling and partially deterministic methods) implemented in MCNP4C could be used depending on the objectives and expected outcome of the simulation.

Table 1. Summary of x-ray CT scanner design parameters used for creation of model geometry as MCNP4C input file.

Gantry		Detector		X-ray tube		Phantom	
Parameter	Option	Parameter	Option	Parameter	Option	Parameter	Option
Source-to-isocentre distance	–[a]	Detector configuration	Single-slice multi-slice, flat panel	X-ray spectra	Full simulation, pre-computed	Phantom type	Shape based, voxel based[b]
Source-to-detector distance	–[a]	Number of detector rows	1, 2, 4, 8, 12, 16, 32, 64	Target angle Target material	–[a] –[a]	Phantom shape	–[a]
Source to primary collimator distance	–[a]	Number of detector elements per row	[a](<1000)	Inherent filtration	Al, Cu,[a]	Phantom dimensions	–[a]
Source to secondary collimator distance	–[a]	Detector element dimensions	–[a]	Additional filter	Al, Cu,[a]	Phantom material	–[a]
Secondary collimation aperture	Circular, rectangular	Ratio of detector element to septa pitch	–[a]	Spectrum energy bin	–[a]	Non-homogeneous phantoms	Yes
Bow-tie filter size	–[a]	Septa element size	–[a]	Focal spot size	–[a]		
Bow-tie filter material	Teflon, PMMA, ... etc	Detector material	Highlight, GOS, CdWO4, CSI				
Beam geometry	Fan-beam, cone-beam	Detector output	Energy deposit, flux				
Beam angle	–[a]	Detector cells geometry	Individual cells, lattice				
Rotation angle	Full, partial rotation						
Number of views	–[a]						

[a] Adjustable.
[b] Under development.

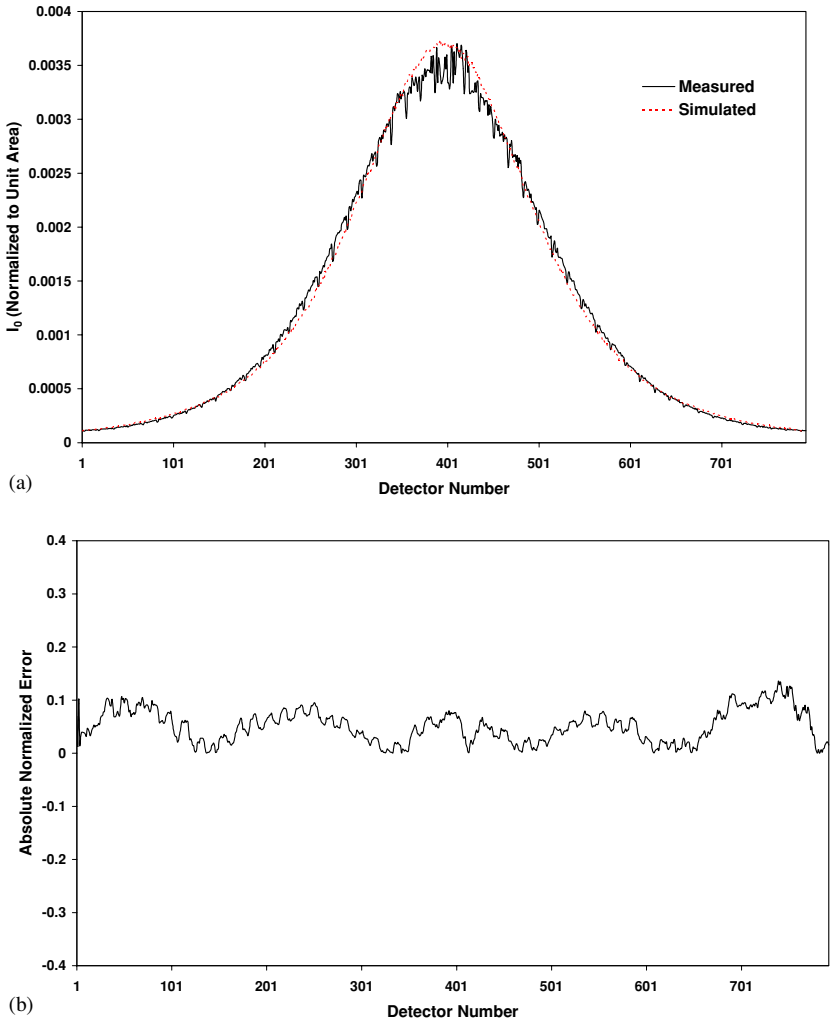

Figure 1. (a) Comparison of simulated and measured bow-tie filter profiles for the GE HiSpeed X/iF CT scanner at tube voltage 120 kV, slice thickness 10 mm and focal spot 1.2 mm. (b) Plot of the absolute normalized error (NE) for the profile shown in (a).

2.2. CT simulator evaluation and validation

The validity of MCNP4C-based Monte Carlo simulator was verified by comparing the simulated and measured distributions from various uniform and non-uniform phantoms on both a fan- and a cone-beam x-ray CT scanner.

2.2.1. Fan-beam human CT scanner. The single-slice GE HiSpeed X/iF CT scanner with Highlight ($Y_2Gd_2O_3$:Eu) ceramic scintillator was used. This third generation CT scanner has 541 mm source-to-isocentre and 949 mm source-to-detector distances, 816 detector elements (793 active elements) with a physical dimension of 0.8 mm. The Highlight scintillator combined with 0.2 mm septa results in a geometrical efficiency of 80%. The actual shape and size of the Teflon bow-tie filter was measured directly on the scanner and used as input to the

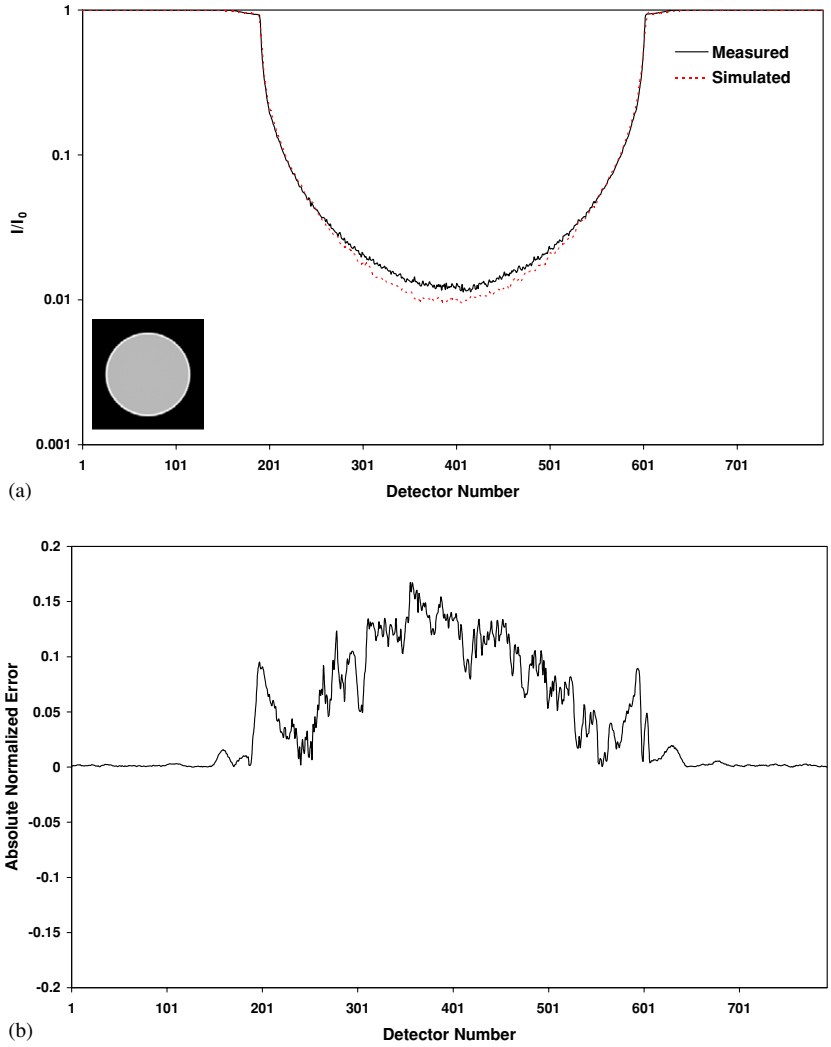

Figure 2. Comparison between simulations and experimental measurements for the GE HiSpeed X/iF CT scanner using the same set-up as in figure 1. (a) Profile of the water phantom. (b) The absolute normalized error of the profile shown in (a). (c) The scatter to primary ratio limited to the field of view.

simulator. The CT scanner is equipped with Solarix x-ray tube with 61.5° fan-beam angle, 7° target angle and minimum inherent filtration of 1.2 mm Al_{eq} at 140 kV.

2.2.2. Cone-beam small-animal CT scanner. The cone-beam small-animal CT scanner is the SkyScan 1076 with 172 mm source-to-detector and 51 mm isocentre-to-detector distances. The x-ray tube is L8032 micro-focus (Hamamatsu Photonics K. K., Iwata City, Japan) with 100 μm Be window and 500 μm aluminium additional filter. The emission cone angle is 39°, the fan angle or angle of the beam in the transaxial plane is 32° while it reduces to 8° in the axis of scanner (cone angle). The scanner uses GOS (Gd_2O_2S) scintillator crystal with 0.025 mm thickness and 100 × 25 mm^2 detector area with pixel size of 12.5 × 12.5 μm^2.

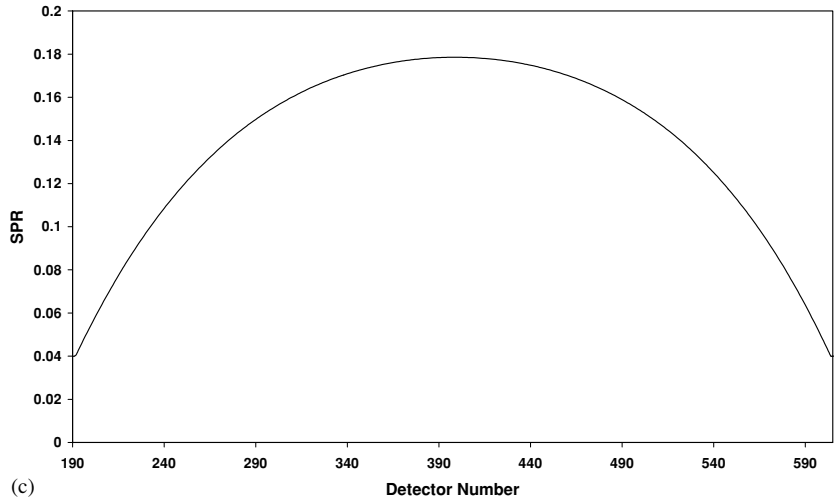

(c)

Figure 2. (Continued.)

The experimental measurements used in this work were taken from a recent paper by Colijn *et al* (2004) related to the validation of their rapid Monte Carlo-based Micro-CT simulator.

2.2.3. Phantoms. Two cylindrical phantoms were constructed specifically for experimental measurements on the clinical fan-beam CT scanner: (i) a homogenous cylindrical water phantom ($\phi 266 \pm 0.5$ mm) with 16 mm acrylic case and (ii) a polyethylene cylindrical phantom ($\phi 200 \pm 0.5$ mm) containing two centred air ($\phi 50 \pm 0.5$ mm) and steel ($\phi 10 \pm 0.5$ mm) cylinders. Another non-uniform software phantom was specifically designed to study the capability of the simulator to produce typical expected profiles when using different materials. This water-filled elliptical cylinder with 220 mm and 80 mm long and short axes, respectively, and 200 mm height contains nine cylinders ($\phi 10$ mm) filled with air ($\rho = 0.0012$ g cm^{-3}), inflated lung ($\rho = 0.296$ g cm^{-3}), deflated lung ($\rho = 1.092$ g cm^{-3}), soft tissue ($\rho = 1.04$ g cm^{-3}), cartilage ($\rho = 1.1$ g cm^{-3}), trabecular bone ($\rho = 1.3$ g cm^{-3}), cortical bone ($\rho = 1.92$ g cm^{-3}), dental implant ($\rho = 4.42$ g cm^{-3}) and hip implant ($\rho = 4.52$ g cm^{-3}).

Three cylindrical phantoms were used for experimental validation of the cone-beam CT scanner (Colijn *et al* 2004): (i) a cylindrical water phantom ($\phi 60$ mm), (ii) the same cylindrical water phantom containing four Teflon rods with 10 mm and 3 mm diameters and (iii) again the same cylindrical water phantom containing two 10 mm Teflon rods and two 3 mm stainless steel rods. The casing of the phantoms was 1 mm polystyrene. The rods were placed along the axial direction of the phantom with equal distance from the cylinder centre.

The normalized error (NE) calculated for each detector element was used as a figure of merit to assess discrepancies between measured and simulated projections using the following formulation (Colijn *et al* 2004):

$$\mathrm{NE}(u, v) = \frac{P_{\mathrm{Measured}}(u, v) - P_{\mathrm{Simulation}}(u, v)}{P_{\mathrm{Measured}}(u, v)} \tag{1}$$

where u and v are detector element's coordinates, $P_{\mathrm{Measured}}(u, v)$ and $P_{\mathrm{Simulation}}(u, v)$ are the measured and simulated projection data for each detector element. To reduce statistical

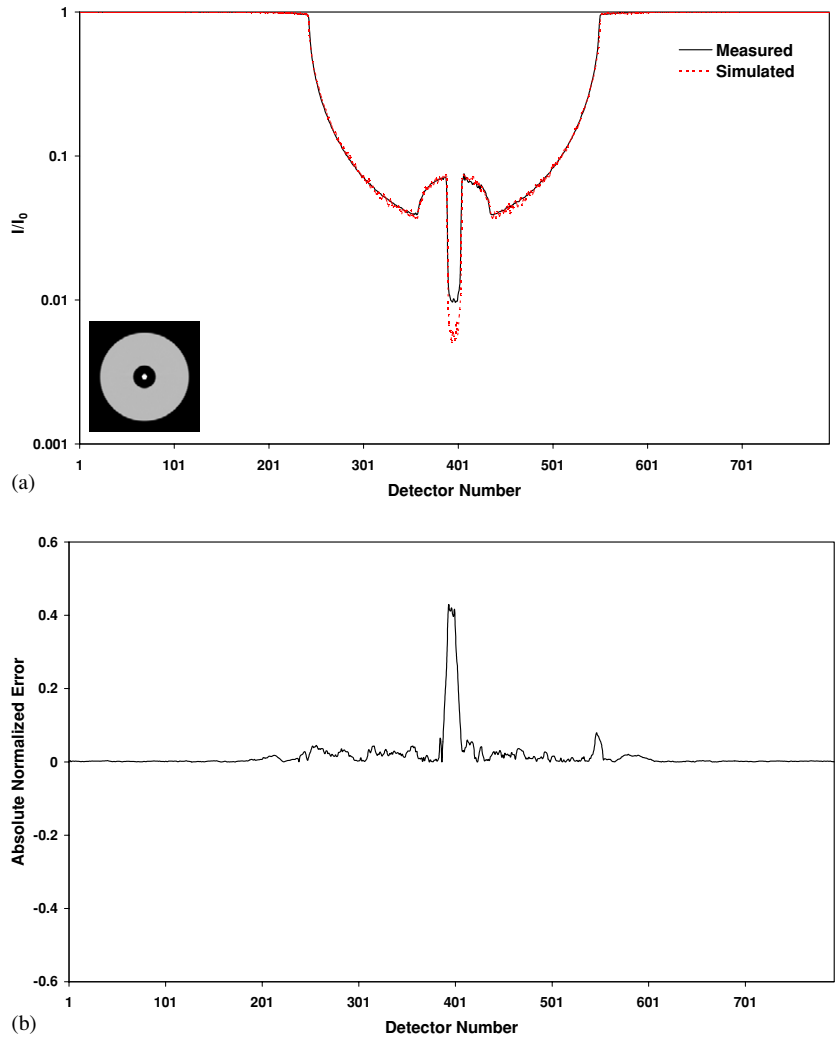

Figure 3. Comparison between simulations and experimental measurements for the GE HiSpeed X/iF CT scanner using the same set-up as in figure 1. (a) Profile of the polyethylene inhomogeneous phantom. (b) The absolute normalized error of the profile shown in (a). (c) The scatter-to-primary ratio limited to the field of view.

fluctuations and quantum noise, the normalized errors were smoothed using eight neighbouring points averaging.

2.3. Characterization of scatter distribution

The corruption of projection data in fan-beam CT scanners with scattered photons was investigated qualitatively by assessing the distribution of scattered photons as a function of phantom size and quantitatively by calculating scatter-to-primary ratio (SPR) for each detector element. Moreover, the effect of septa length on the scatter profile using full transport of photons inside the septa plates was studied. Statistical fluctuations in the scatter projections were removed for visualization using least-square polynomial fits having

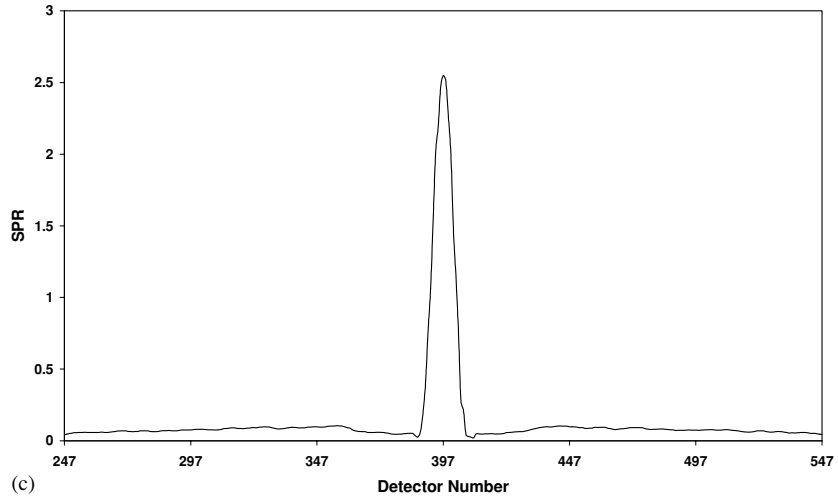

(c)

Figure 3. (Continued.)

the highest order polynomial that was practical by means of the XPlot software (European Synchrotron Radiation Facility, France). In all cases, $\sim 1.9 \times 10^9$ photons were simulated from the focal spot where $\sim 4.4 \times 10^7$ photons could pass through the bow-tie filter, primary and secondary collimator blades. Increasing the number of photon histories will decrease the statistical fluctuations and quantum noise in the simulated profiles and thus decrease the standards deviations of the estimates. We made every effort to match the simulated statistical fluctuations to the range found in measured results.

3. Results

3.1. Validation

3.1.1. Fan-beam human CT scanner. Figure 1 shows the comparison between measured and simulated blank scan profiles (detector elements output without phantom being present) from the GE HiSpeed X/iF scanner. The bell shape of the profile is due to photons attenuation on the edges by the Teflon bow-tie filter. This profile was used for blank scan correction to compensate for detectors response non-uniformity in the results presented in the following figures. The absolute normalized error for each detector element is also shown. The maximum of absolute normalized error and average normalized errors in the blank scan profile are 13% and 1.1%, respectively.

The comparison of simulated and measured cylindrical water-filled phantom profiles is shown in figure 2. Both measured and simulated profiles were divided by the corresponding blank scan illustrated in figure 1 (blank scan correction). The log-linear scale was used to magnify the differences between simulated and measured profiles in the central area of the phantom where attenuation lengths are maximum (figure 2(a)). Likewise, the absolute normalized error for each detector element is also shown (figure 2(b)). The noticeable peaks on the borders of the phantom are due to slight misalignment between simulated and measured phantoms (maximum = 16.3%). The central region in the scatter-to-primary ratio plot for detector elements covered by the phantom is larger owing to the smaller number of detected primary photons in this area (figure 2(c)).

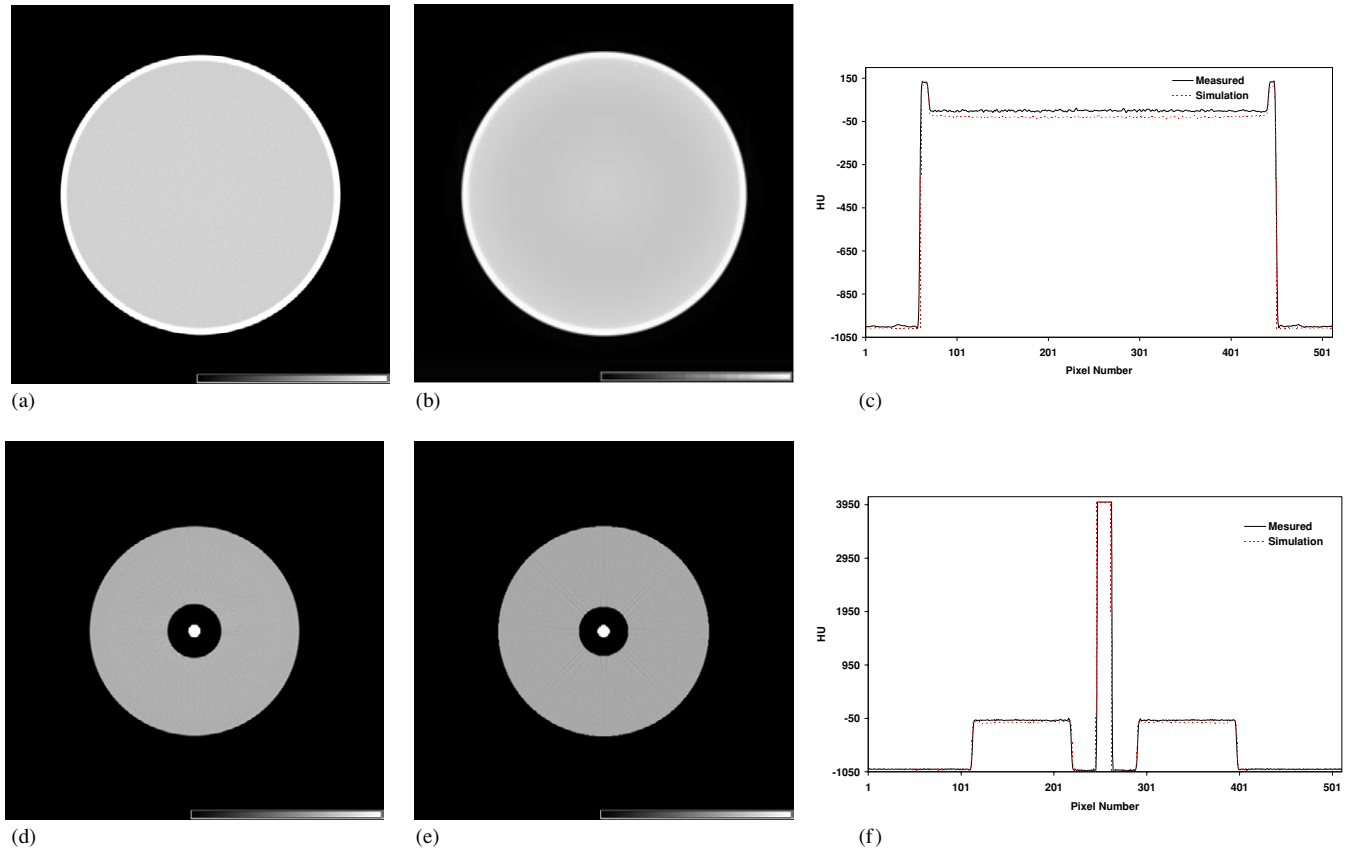

Figure 4. Representative images of the measured cylindrical water phantom reconstructed using commercial software (a) and simulated cylindrical water phantom reconstructed using *ifanbeam.m* FBP Matlab routine (b) together with a comparison of central horizontal profiles between measured and simulated image are shown (c). Same as above for the inhomogeneous polyethylene phantom illustrating measured (d) and simulated (e) images and horizontal profiles (f). The window level and width were set at –200 and 600 HU, respectively, for both images.

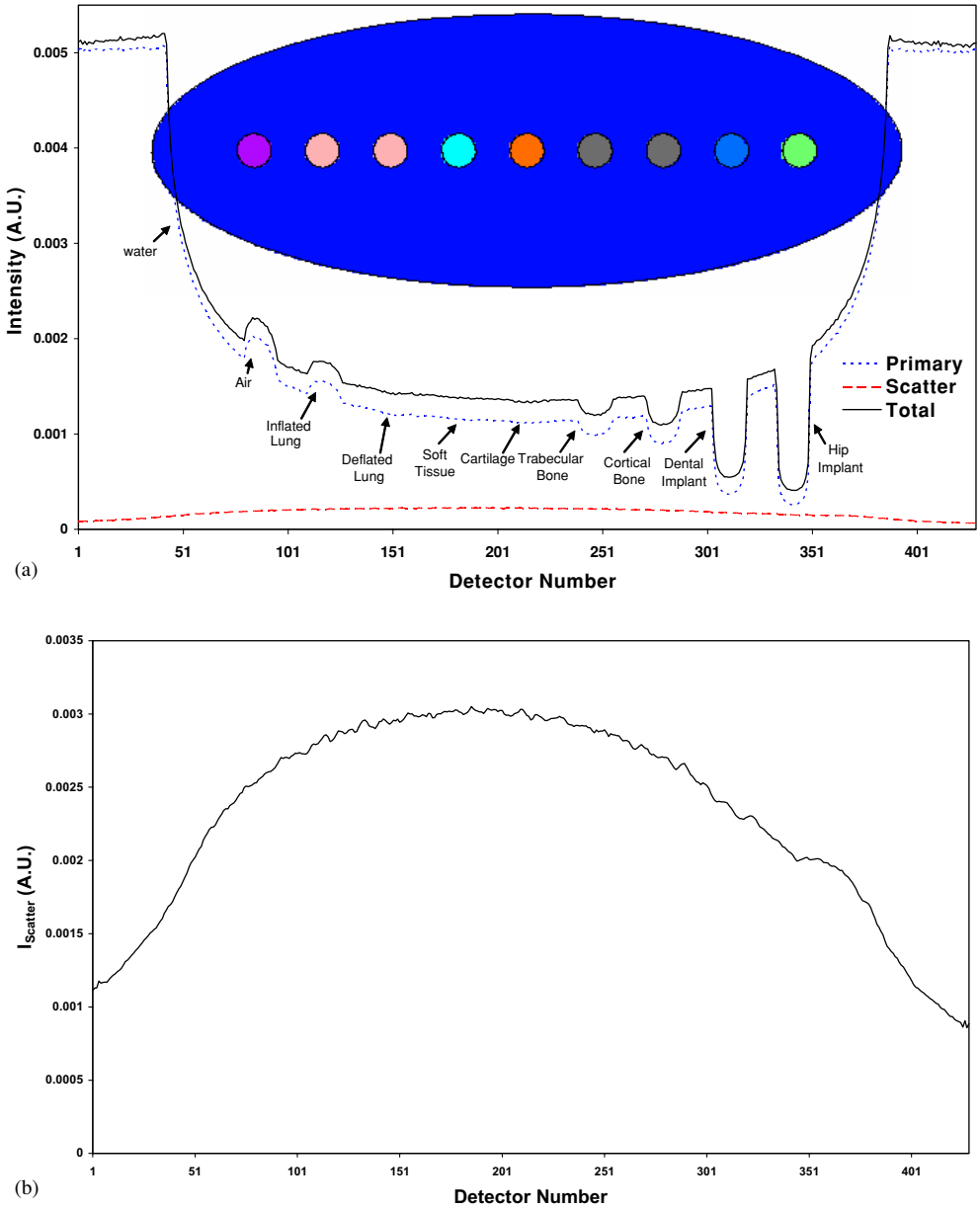

Figure 5. Simulated profiles of the water-filled elliptical phantom containing nine cylindrical inserts filled with different materials showing (a) total detected events (full line) separated into different contributions due to primary (dotted line) and scattered (dashed line) photons. (b) Magnified spatial distribution of scattered photons is shown for clarity.

Figure 3 shows the comparison between simulated and measured profiles of the polyethylene cylindrical phantom containing air and steel cylinders after blank scan correction. Good agreement between the simulated and measured profiles can be observed in the polyethylene and air regions of the phantom (figure 3(a)). The maximum absolute normalized error (42%) occurs in the area corresponding to the central steel rod (figure 3(b)). The

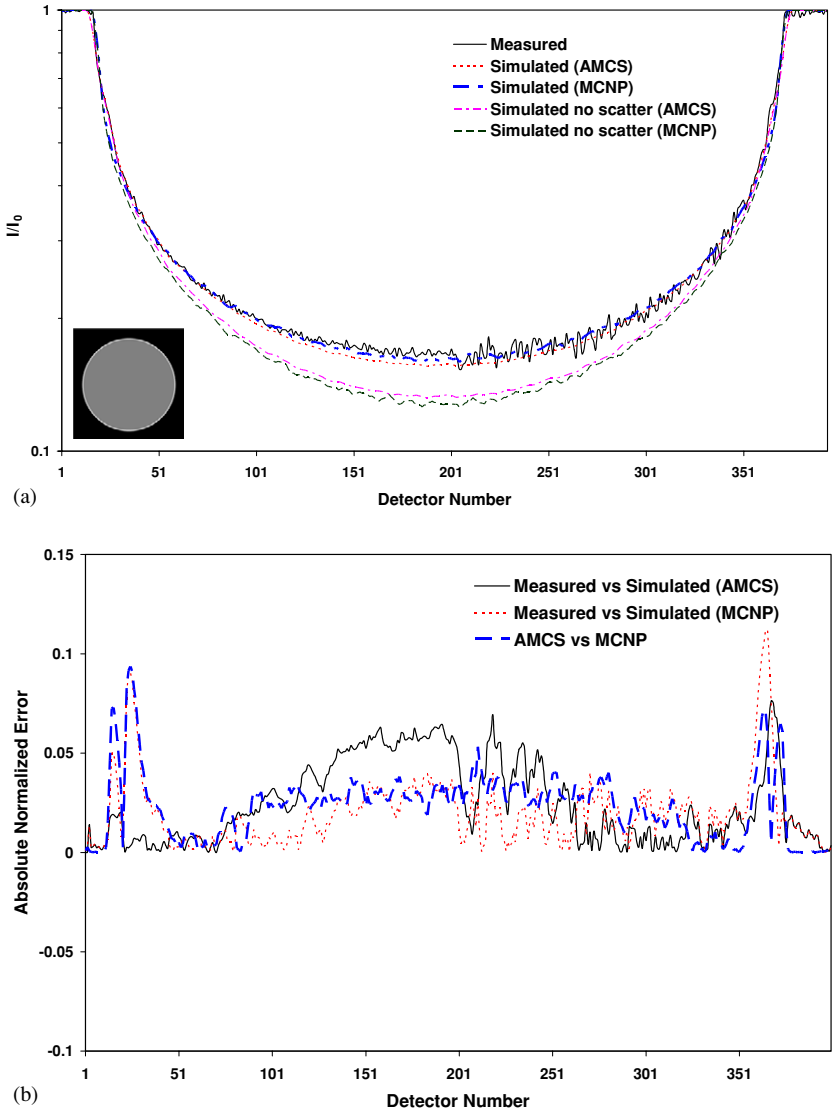

Figure 6. Comparison between MCNP and AMCS simulated profiles and experimental measurements of the water phantom (Colijn *et al* 2004) using the SkyScan small-animal x-ray CT scanner at tube voltage 100 kV showing (a) total and primary profiles; (b) the absolute normalized error of the profiles shown in (a); and (c) the scatter-to-primary ratio for the simulated data.

high scatter-to-primary ratio peak (maximum = 255%) observed in the central part could be explained by the high absorption of primary photons in the steel rod (figure 3(c)).

The images of the real and simulated water and polyethylene phantoms reconstructed using filtered back-projection reconstruction algorithm as implemented in commercial software incorporating beam hardening and scatter correction and Matlab's *ifanbeam.m* routine after beam hardening removal from the projections (Kanamori *et al* 1985), respectively, together with a central horizontal profile from reconstructed images are shown in figure 4. The

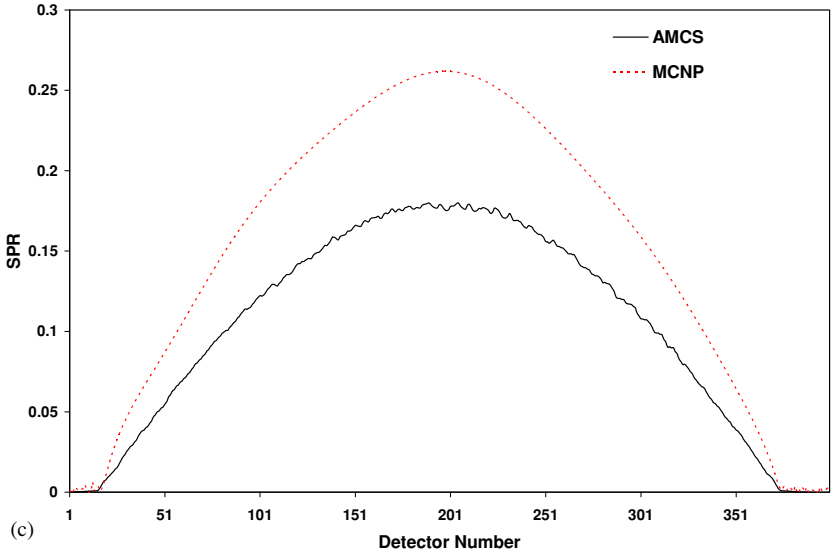

(c)

Figure 6. (Continued.)

underestimation of CT numbers in simulated images is due to contribution from scattered radiation, which is corrected for during the reconstruction process in measured images using software supplied by scanner manufacturers. The contrast detectability of MCNP4C-based simulator was further investigated in figure 5, which shows the total, primary and scatter profiles of simulated elliptical water-filled cylindrical phantom containing nine cylinders filled with different materials. The magnified scatter profile is also shown separately. It should be emphasized that a CT geometry with 430 detector elements, 60° fan angle, 5 mm septa length and 80% geometrical efficiency was used for the calculation of these profiles by simulating 10^9 photon histories sampled from the 140 kV spectrum with 2 mm Al filter. Although the effect of deflated lung, soft tissue and cartilage is not clearly distinguishable on the profiles, it is expected that the simulation of a large number of photon histories would help us to resolve materials having small differences in electronic density.

3.1.2. Cone-beam small-animal CT scanner. Figures 6–8 show the comparison of MCNP4C simulated and measured profiles from the SkyScan 1076 cone-beam small-animal CT as well as the simulated profiles using the AMCS micro-CT simulator (Colijn *et al* 2004). The simulated flat detector configuration was considered as a 400 × 100 grid of 250 × 250 μm^2 detector elements area. The profiles were calculated from the central row of detector matrix. The unscattered profiles were calculated by removing the scattered photons contribution from the simulated profiles. There is generally good agreement between both MCNP4C- and AMCS-based simulations and experimental results. The calculated absolute normalized error for each detector element shows that the MCNP4C-based simulator is in better agreement with measured profiles in comparison to AMCS with a maximum absolute normalized error of 4% in the area covered by the phantom (figure 6(b)). The maximum scatter-to-primary ratios calculated using MCNP4C and AMCS are 26% and 18%, respectively (figure 6(c)). The discrepancy between MCNP4C and AMCS simulation results appears to be due to underestimation of the scattered component and overestimation of primary component by AMCS in comparison with MCNP4C.

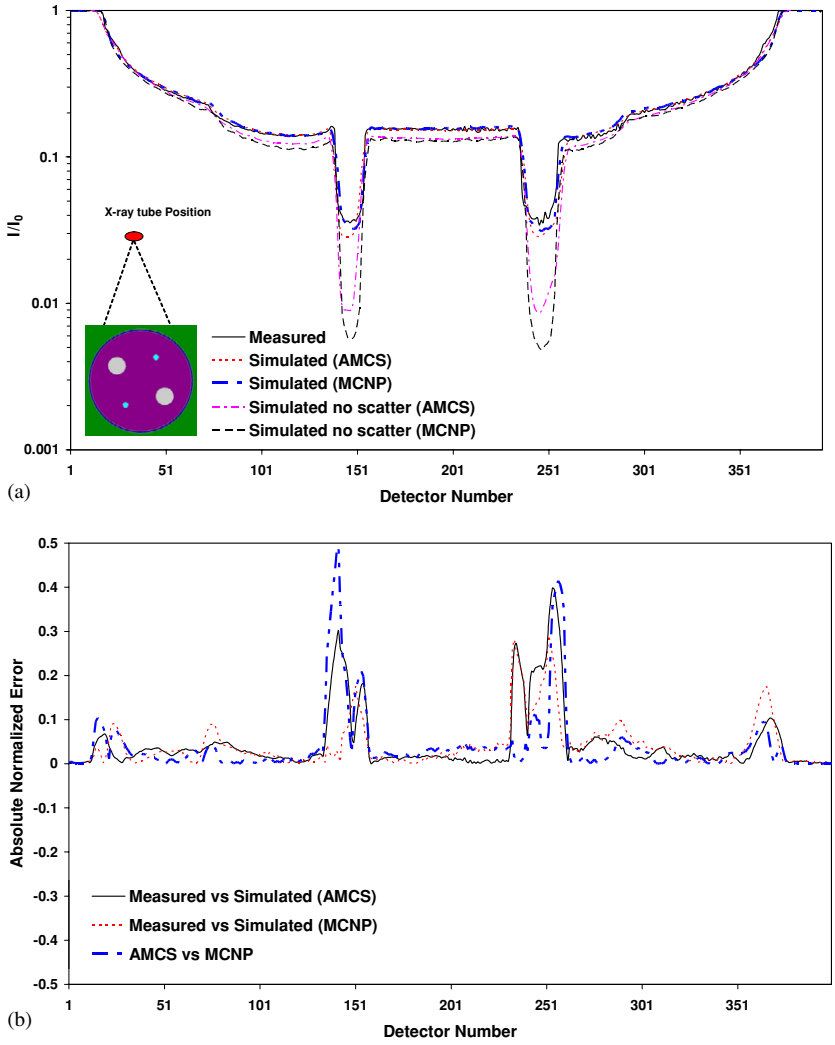

Figure 7. Comparison between MCNP and AMCS simulated profiles and experimental measurements from water phantom containing steel and Teflon rod inserts (Colijn *et al* 2004) using the SkyScan small-animal x-ray CT scanner at tube voltage 100 kV showing (a) total and primary profiles; (b) the absolute normalized error of the profiles shown in (a); and (c) the scatter-to-primary ratio for the simulated data.

Figure 7 shows the comparison of measured and simulated profiles from water phantom containing Teflon and steel rods presented in log-linear scale in order to magnify the differences between simulated and measured results. It appears that MCNP4C has better agreement with the measured profile compared to AMCS (figure 7(b)). The high absolute normalized error in the area covered by steel rods is due to the high attenuation of steel and probably small geometrical misalignment between simulated and experimental set-ups. The comparison between calculated SPR further illustrates the discrepancy between AMCS and MCNP4C in the region corresponding to steel rod location for the reasons discussed above (figure 7(c)). Figure 8 shows the comparison of simulated and measured profiles, absolute normalized error

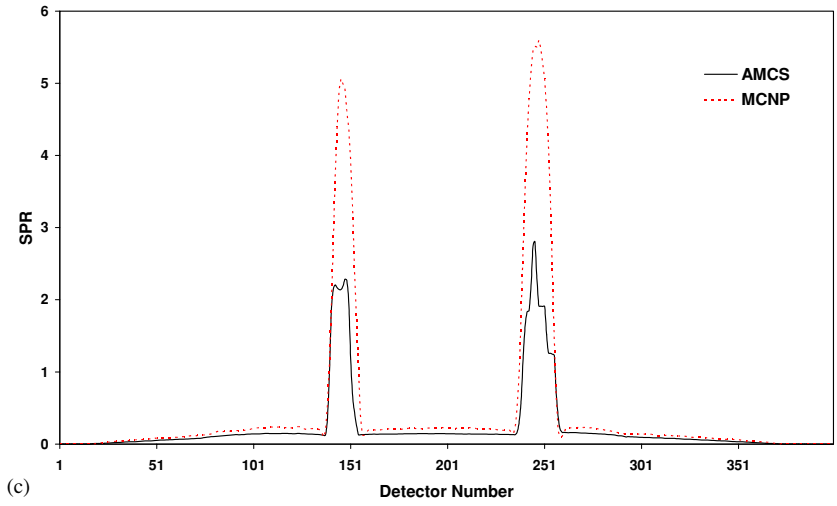

(c)

Figure 7. (Continued.)

and SPR for the water-filled phantom containing four Teflon rods. There is generally good agreement between MCNP4C-simulated profiles and measured and AMCS-simulated profiles whereas the same conclusions regarding the SPR still hold.

3.2. Scatter characterization

To characterize the spatial distribution of scattered photons from the bow-tie filter and objects of different size, corresponding scatter profiles calculated using the Monte Carlo simulator for the geometry of the fan-beam GE HiSpeed X/iF CT scanner are shown in figure 9. The scatter profile of the blank scan illustrates the detected photons following interaction within the bow-tie filter only whereas the remaining profiles reflect different combinations of detected scattered radiation from the water-filled phantom and bow-tie filter. It can be seen that the scatter profile follows closely the phantom size in the presence of Teflon bow-tie filter (figure 9(b)). The scatter profile in the region corresponding to the phantom decreases with increasing the phantom size as a result of increasing the attenuation length compared to the photons' mean free path.

In fan-beam CT scanners, the collimator (septa) in the detector housing directed towards the focal spot is generally used to decrease the contribution of scattered radiation. The corruption of x-ray projection data with scattered radiation decreases by increasing septa length. Figure 10 shows the effect of septa length on the scatter profile obtained by simulating a cylindrical water phantom (ϕ266 mm) in presence of bow-tie filter together with the relative number of detected total, primary and scattered photons. The relative difference between detected total, primary and scatter photons for septa length varying between 0 and 95 mm is 11.2%, 1.9% and 84.1%, respectively, whereas the scatter-to-primary ratio decreases by 83.8%.

4. Discussion

The MCNP4C-based x-ray CT simulator developed in this work is in good agreement with both experimental measurements performed on clinical and small-animal CT scanners and

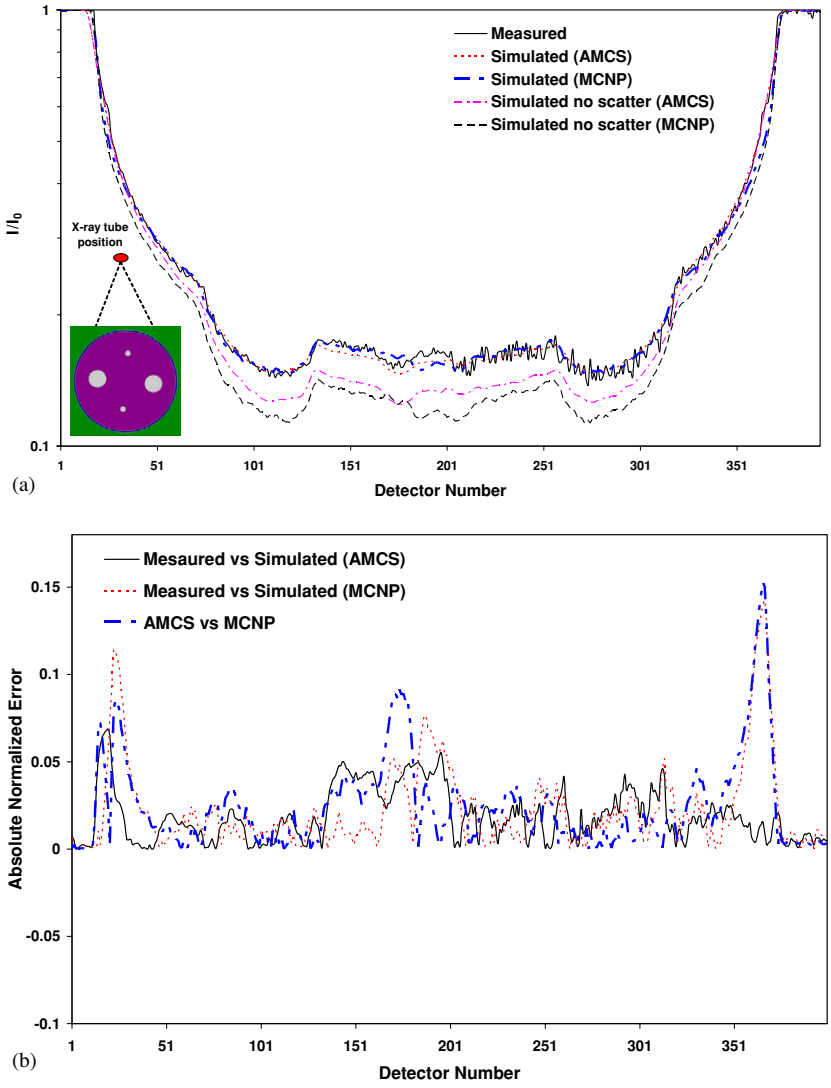

Figure 8. Comparison between MCNP and AMCS simulated profiles and experimental measurements from water phantom containing 4 Teflon rods (Colijn *et al* 2004) using the SkyScan small-animal x-ray CT scanner at tube voltage 100 kV showing (a) total and primary profiles; (b) the absolute normalized error of the profiles shown in (a); and (c) the scatter-to-primary ratio for the simulated data.

similar simulated results obtained using an independent dedicated simulator. Therefore, it could serve as an excellent tool for detailed investigation of the effect of different scanner design parameters and data correction techniques on resulting image quality. In the following paragraphs, the origins of small discrepancies between simulated and measured results are discussed.

The discrepancy observed in the blank scan profiles (figure 1) can be explained by apparent differences between the real complex shape of the scanner's bow-tie filter and that used as input to the simulator modelled using combinations of ellipsoidal and cubic surfaces. Although the

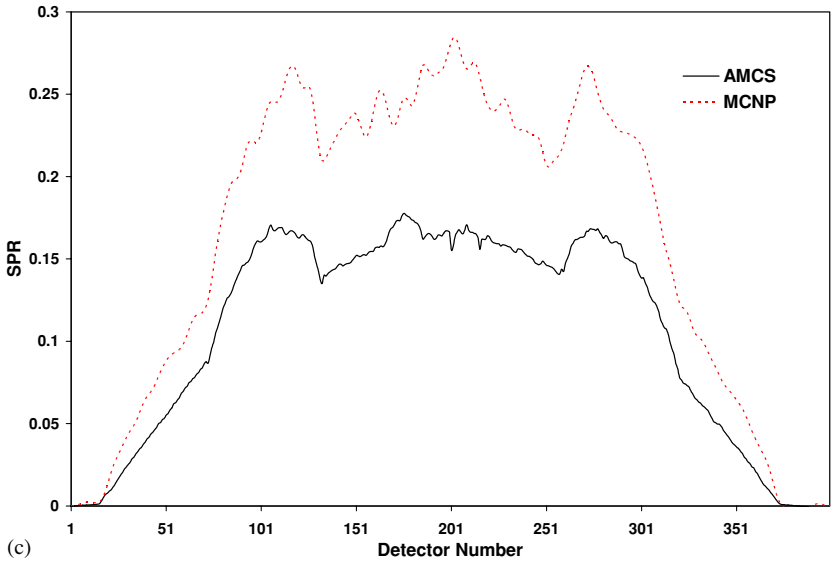

(c)

Figure 8. (Continued.)

average normalized error in the blank scan profile is ∼1.1%, the maximum is close to 13%, which can bias somehow the generated data since each simulated x-ray projection data should be divided by the blank scan to compute attenuation profiles. More elaborate modelling of the bow-tie filter should help decreasing the discrepancy, thus preventing error propagation to the simulated projections. Likewise, the small discrepancy between the measured and simulated projections of the cylindrical water phantom (figure 2) is due to differences in the central area of the corresponding measured and simulated blank scans. It has been shown that the distribution of scattered photons in the cylindrical water phantom is approximately uniform. The curvature of SPR (figure 2(c)) is due to the variable probability of primary photons transmission, which is significantly lower in the region corresponding to longer path lengths (central area). The discrepancy between the simulated and measured profiles of the polyethylene phantom (figure 3(a)) arises from two crucial factors: firstly the density and chemical composition of the simulated and commercially available (mixed) steel were not similar (pure steel was simulated); and secondly the high attenuation of steel in the x-ray spectra energy range decreases the probability of photons transmission, thus increasing the statistical uncertainty in the region covered by steel. The high value of SPR in the steel area (figure 3(c)) is due to the high absorption of primary photons in the steel since the scatter distribution is approximately uniform.

The good agreement between simulated and measured images is an additional proof of the accurate modelling of x-ray CT imaging physics incorporated in the Monte Carlo simulator and associated user interface program (figure 4). It should be noted that the simulated projection data were reconstructed without performing scatter correction in contrary to the experimentally measured data where the commercial reconstruction software supplied by the manufacturer was used to effectively remove scatter artefacts. The central horizontal profiles revealed slight underestimation of CT numbers in simulated images as compared to the measured images, which is due to contribution of scattered photons. The low and high contrast detectability of the x-ray CT simulator was also investigated demonstrating modest performance for low contrast detectability depending on the collected statistics (figure 5).

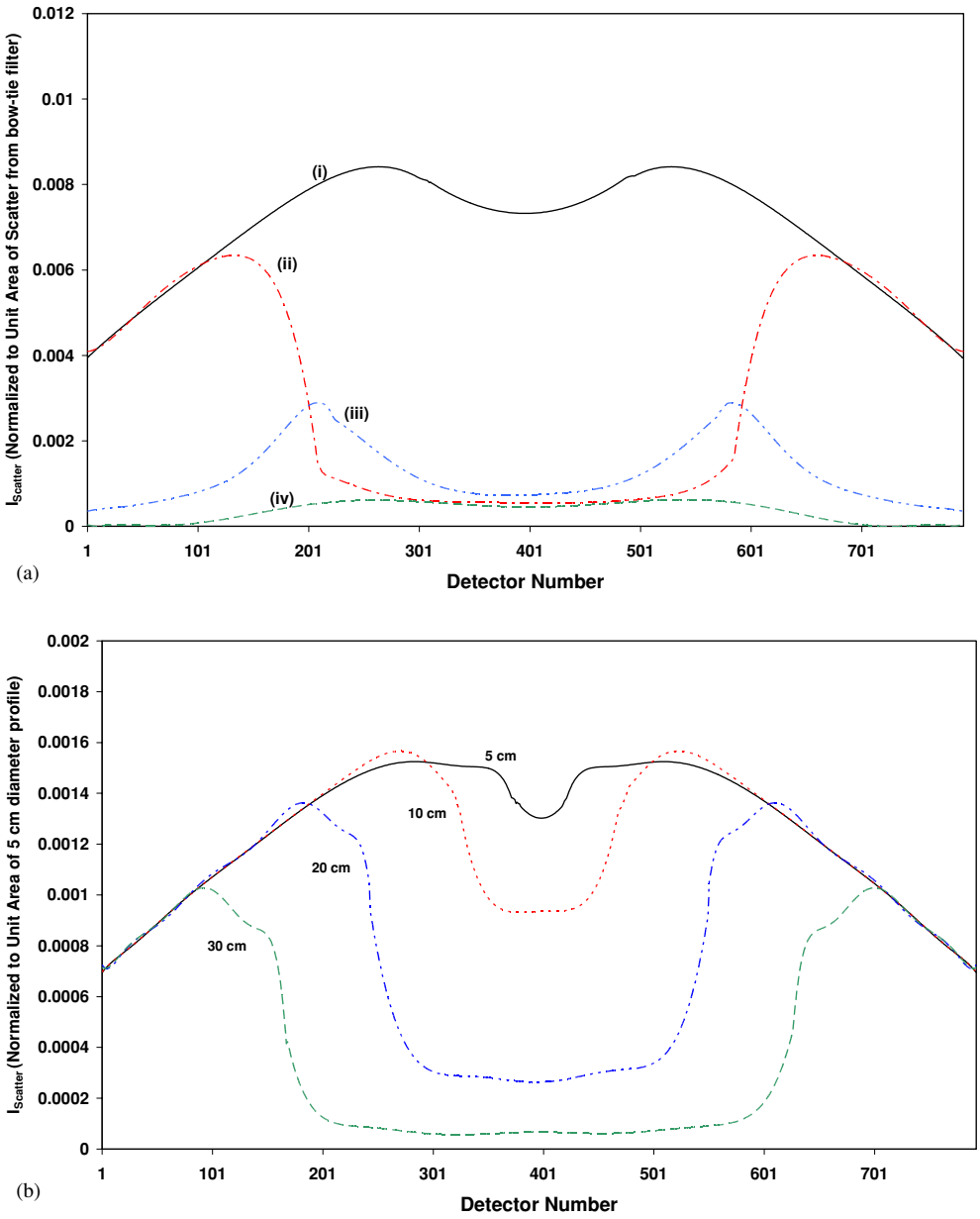

Figure 9. Simulated scatter profiles for the GE HiSpeed X/iF CT scanner using the same set-up as in figure 1 for (a) blank scan with bow-tie filter (without water phantom) (i), water phantom and bow-tie filter (ii), water phantom without bow-tie filter (iii), and only Compton scattering in the water phantom (in the presence of bow-tie filter) (iv); (b) cylindrical water phantoms with different size.

There is generally good agreement between measured and simulated results using both MCNP4C and AMCS for the cone-beam small-animal CT scanner (figures 6–8). The absolute normalized error plots for different phantoms demonstrated that MCNP4C has better agreement with measured projections in comparison to AMCS. Although the SPR estimates using both

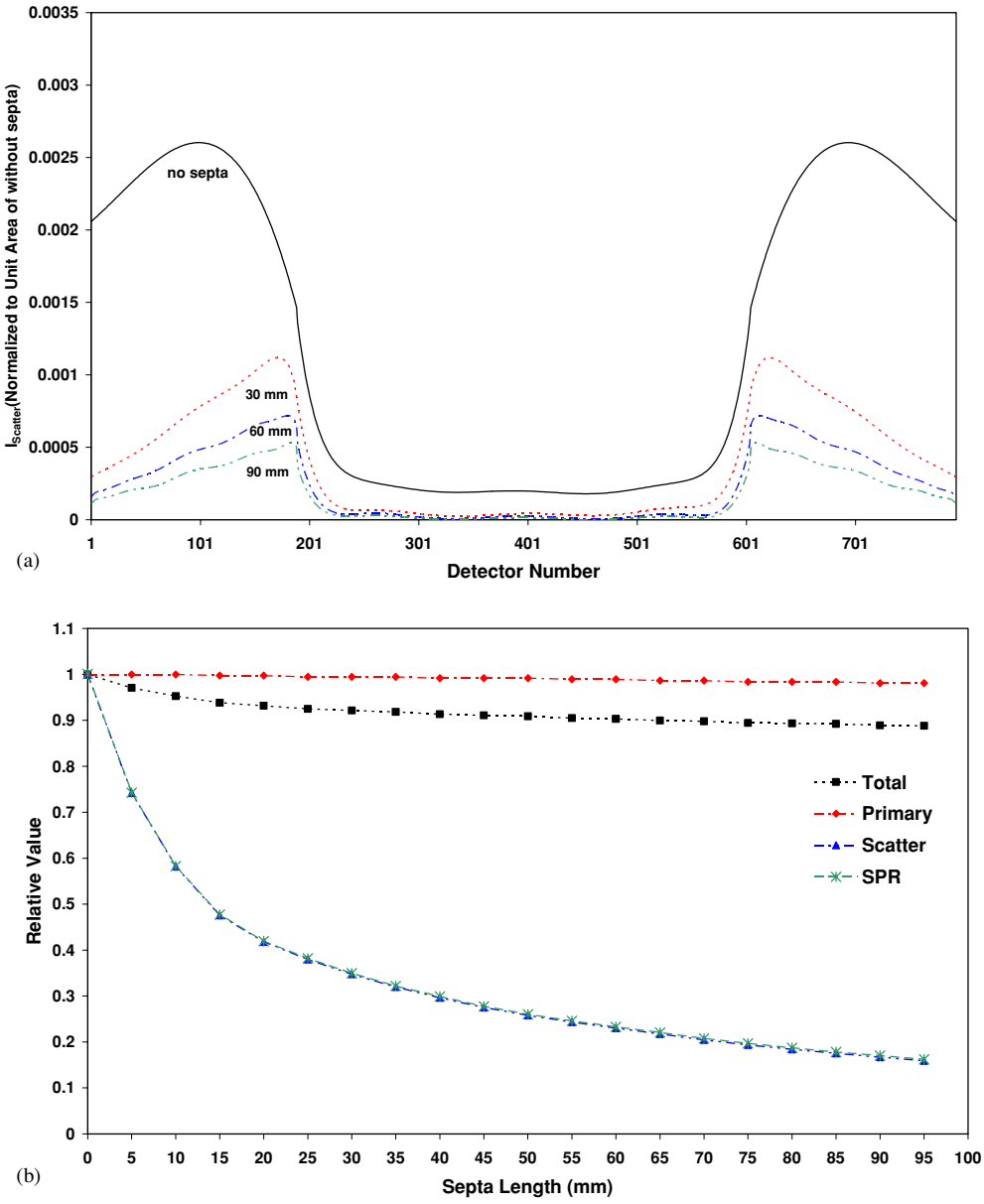

Figure 10. Monte Carlo simulations of the cylindrical water phantom for the GE HiSpeed X/iF CT scanner using the same set-up as in figure 1 showing both (a) simulated scatter profiles and (b) relative SPR, total, primary and scattered photons, as a function of septa length.

simulation programs have the same shape, there is a substantial discrepancy in the magnitude of the profile which can be explained by the underestimation of the scattered component and overestimation of primary component by AMCS. In the absence of gold standard with respect to the contribution of primary and scattered photons to the projection data, it is difficult to judge the validity of both computational codes. However, the better agreement of the MCNP4C-based CT simulator with experimental measurements could be an indicator of its

improved performance. It should also be emphasized that AMCS uses XCOM photon cross section libraries (Berger and Hubbell 1987) whereas the scattering cross sections in MCNP are taken from ENDF tabulations (Hubbell *et al* 1975). In addition, AMCS combines short Monte Carlo simulation with data fitting and other acceleration techniques to generate noise-free scatter projections (Colijn and Beekman 2004), which might introduce an additional uncertainty.

It has been shown that scatter in the bow-tie filter used in fan-beam CT scanners to reduce dynamic range requirements for the detector and to decrease the radiation dose to the patients contributes significantly to the scatter component (figure 9). The two peaks in the scatter profile are due to the trade-off between increasing the probability of Compton scattering while decreasing the transmission probability of scattered photons from the bow-tie filter with increasing the attenuation length. It should be noted that the lower scattered photons at the centre of the profile covered by the phantom (whose diameter is large compared to the mean free path of photons) is the result of either absorption of incoming photons before undergoing Compton scattering or their absorption after undergoing Compton scattering. The set-up used to assess the scatter profile without bow-tie filter being present corresponds to the configuration adopted by Johns and Yaffe (1982) to measure experimentally the scatter profile. Consistent with the observations made by Glover (1982), the bow-tie filter decreases the scatter component in the region covered by the phantom. Increasing the septa length could effectively reduce the contribution of scattered radiation, thus decreasing the scatter-to-primary ratio (figure 10). The optimal septa length to be used in the design of multi-slice CT scanners is still an open research question, which requires further research and development efforts.

It should be noted that the x-ray CT simulator described in this paper is still time consuming ($\sim$1 h per view—depending on complexity of the geometry—on a medium performance single processor PC), which is not a major concern in a research environment where massively parallel computers, PC clusters and Grid technology are generally available. Recently, we attempted to generate images using a combination of techniques including pure Monte Carlo and analytic models resulting in a hybrid approach namely numerical approaches using Monte Carlo data which seems to be reliable thus allowing us to reduce significantly the computation time.

5. Conclusion

An MCNP4C-based Monte Carlo simulator for fan- and cone-beam x-ray CT with single-slice, multi-slice and flat detector configurations has been developed. A user interface program running under Matlab 6.5.1 was designed to create the geometry of the actual CT scanner as MCNP's input file and perform image reconstruction of the simulated projection data. The simulated projections of various phantoms for both human and small-animal CT scanners were in good agreement with experimentally measured and published simulated data. Likewise, the reconstructed images were also comparable to the images obtained from the measured projections. The developed x-ray CT simulator is a powerful tool for evaluating the effect of physical, geometrical and other design parameters on the performance of new generation CT scanners and image quality in addition to offering a versatile tool for optimizing the absorbed dose to the patients and investigating potential artefacts and optimal correction schemes when using CT-based attenuation correction on dual-modality PET/CT units (Hasegawa and Zaidi 2005) in connection with ongoing research in our lab related to PET quantification using a dedicated PET Monte Carlo simulator (Zaidi *et al* 1999).

Acknowledgments

This work was supported by the Swiss National Science Foundation under grant SNSF 3152A0-102143. The authors would like to thank W Zbijewski, H Ghadiri and H Moosavi for providing some of the data used in this work, F Schoenahl and M Adib for their support in programming and D Keidel from GE Healthcare Technologies for supplying design parameters of the HiSpeed X/iF CT scanner.

References

Atherton J V and Huda W 1995 CT dose in cylindrical phantoms *Phys. Med. Biol.* **40** 891–911

Ay M R, Shahriari M, Sarkar S, Adib M and Zaidi H 2004 Monte Carlo simulation of x-ray spectra in diagnostic radiology and mammography using MCNP4C *Phys. Med. Biol.* **29** 4897–917

Ay M R, Sarkar S, Shahriari M, Sardari D and Zaidi H 2005 Assessment of different computational models for generation of x-ray spectra in diagnostic radiology and mammography *Med. Phys.* **32** 1660–75

Berger M J and Hubbell J H 1987 *XCOM: Photon Cross Sections on a Personal Computer* National Bureau of Standards (US)

Boone J M, Cooper V N, Nemzek W R, McGahan J P and Seibert J A 2000 Monte Carlo assessment of computed tomography dose to tissue adjacent to the scanned volume *Med. Phys.* **27** 2393–407

Briesmeister J F 2000 *MCNP—A General Monte Carlo N-Particle Transport Code Version 4C* (Los Alamos, NM: Los Alamos National Laboratory)

Caon M, Bibbo G and Pattison J 1997 A comparison of radiation dose measured in CT dosimetry phantoms with calculations using EGS4 and voxel-based computational models *Phys. Med. Biol.* **42** 219–29

Caon M, Bibbo G, Pattison J and Bhat M 1998 The effect on dose to computed tomography phantoms of varying the theoretical x-ray spectrum: a comparison of four diagnostic x-ray spectrum calculating codes *Med. Phys.* **25** 1021–7

Chen B and Ning R 2002 Cone-beam volume CT breast imaging: feasibility study *Med. Phys.* **29** 755–70

Colijn A P and Beekman F J 2004 Accelerated simulation of cone beam x-ray scatter projections *IEEE Trans. Med. Imaging* **23** 584–90

Colijn A P, Zbijewski W, Sasov A and Beekman F J 2004 Experimental validation of a rapid Monte Carlo based micro-CT simulator *Phys. Med. Biol.* **49** 4321–33

Cristy M and Eckerman K F 1987 *Specific Absorbed Fractions of Energy at Various Ages from Internal Photon Source* Rep. ORNL/TM-8381/V1-7, Oak Ridge National Laboratory

De Francesco D and Da Silva A 2002 Multislice spiral CT simulator for dynamic cardiopulmonary studies *SPIE Medical Imaging 2002: Physiology and Function from Multidimensional Images (San Diego, CA, USA) SPIE* vol 4683 pp 305–16

De Man B 2001 Iterative reconstruction for reduction of metal artifact in computed tomography *PhD Thesis* Leuven University, Belgium

Drangova M and Fenster A 1994 A laboratory CT scanner for dynamic imaging *Med. Phys.* **21** 731–40

Endo M, Tsunoo T, Nakamori N and Yoshida K 2001 Effect of scatter radiation on image noise in cone beam CT *Med. Phys.* **28** 469–74

Glover G H 1982 Compton scatter effects in CT reconstructions *Med. Phys.* **9** 860–7

Hasegawa B H and Zaidi H 2005 Dual-modality imaging: more than the sum of its components *Quantitative Analysis in Nuclear Medicine Imaging* ed H Zaidi (New York: Springer) pp 35–81

Hsieh J 2003 Analytical models for multi-slice helical CT performance parameters *Med. Phys.* **30** 169–78

Hubbell J H, Veigele W J, Briggs E A, Brown R T, Cromer D T and Howerton R J 1975 Atomic form factors, incoherent scattering functions, and photon scattering cross-sections *J. Phys. Chem. Ref. Data* **4** 471–538

Jarry G, DeMarco J J, Beifuss U, Cagnon C H and McNitt-Gray M F 2003 A Monte Carlo-based method to estimate radiation dose from spiral CT: from phantom testing to patient-specific models *Phys. Med. Biol.* **48** 2645–63

Johns P C and Yaffe M 1982 Scattered radiation in fan beam imaging systems *Med. Phys.* **9** 231–9

Joseph P M and Spital R D 1982 The effects of scatter in x-ray computed tomography *Med. Phys.* **9** 464–72

Kak A C and Slaney M 1999 *Principles of Computerized Tomographic Imaging* (New York: IEEE Press)

Kanamori H, Nakamori N, Inoue K and Takenaka E 1985 Effect of scattered x-ray on CT images *Phys. Med. Biol.* **30** 239–49

Khodaverdi M, Chatziioannou A F, Weber S, Ziemons K, Halling H and Pietrzyk U 2005 Investigation of different microCT scanner configurations by GEANT4 simulations *IEEE Trans. Nucl. Sci.* **52** 188–92

Lee S C, Kim H K K, Chun I K, Cho M H, Lee S Y and Cho M H 2003 A flat-panel detector based micro-CT system: performance evaluation for small-animal imaging *Phys. Med. Biol.* **48** 4173–85

Lucas P A, Dance D R, Castellano I A and Vano E 2004 Monte Carlo simulations in CT for the study of the surface air kerma and energy imparted to phantoms of varying size and position *Phys. Med. Biol.* **49** 1439–54

Malusek A, Sandborg M P and Carlsson G A 2003 Simulation of scatter in cone beam CT: effects on projection image quality SPIE *Medical Imaging 2003: Physics of Medical Imaging (San Diego, CA, USA) SPIE* vol 5030 pp 740–51

Meinel J F, Wang G, Jiang M, Ferei T, Vannier M and Hoffman E 2003 Spatial variation of resolution and noise in multi-detector row spiral CT *Acad. Radiol.* **10** 607–13

Merritt R B and Chenery S G 1986 Quantitative CT measurements: the effect of scatter acceptance and filter characteristics on the EMI 7070 *Phys. Med. Biol.* **31** 55–63

Ohnesorge B, Flohr T and Klingenbeck_Regn K 1999 Efficient object scatter correction algorithm for third and fourth generation CT scanners *Eur. Radiol.* **9** 563–9

Siewerdsen J H and Jaffray D A 2000 Optimization of x-ray imaging geometry (with specific application to flat-panel cone-beam computed tomography) *Med. Phys.* **27** 1903–14

Siewerdsen J H and Jaffray D A 2001 Cone-beam computed tomography with flat-panel imager: magnitude and effects of x-ray scatter *Med. Phys.* **28** 220–31

Storm E and Israel H I 1967 *Photon Cross-Section from 0.001 to 100 MeV for Elements 1 through 100* LA-3753, Los Alamos Scientific Laboratory

Tofts P S and Gore J C 1980 Some sources of artefact in computed tomography *Phys. Med. Biol.* **25** 117–27

Wang L, Lovelock M and Chui C S 1999 Experimental verification of a CT-based Monte Carlo dose-calculation method in heterogeneous phantoms *Med. Phys.* **26** 2626–34

Xu X G, Chao T C and Bozkurt A 2000 VIP-MAN: an image-based whole-body adult male model constructed from color photographs of the visible human project for multi-particle Monte Carlo calculations *Health Phys.* **75** 476–86

Zaidi H, Scheurer A H and Morel C 1999 An object-oriented Monte Carlo simulator for 3D cylindrical positron tomographs *Comput. Methods Prog. Biomed.* **58** 133–45